analytical chemistry

pubs.acs.org/ac Article

Challenging a Preconception: Optoacoustic Spectrum Differs from the Absorption Spectrum of Proteins and Dyes for Molecular Imaging

Juan Pablo Fuenzalida Werner, Yuanhui Huang, Kanuj Mishra, Robert Janowski, Paul Vetschera, Christina Heichler, Andriy Chmyrov, Clemens Neufert, Dierk Niessing, Vasilis Ntziachristos, and Andre C. Stiel*

Cite This: https://dx.doi.org/10.1021/acs.analchem.0c01902 Read Online

ACCESS | Metrics & More | Article Recommendations | Supporting Information

ABSTRACT: Optoacoustic (photoacoustic) imaging has seen marked advances in detection and data analysis, but there is less progress in understanding the photophysics of common optoacoustic contrast agents. This gap blocks the development of novel agents and the accurate analysis and interpretation of multispectral optoacoustic images. To close it, we developed a multimodal laser spectrometer (MLS) to enable the simultaneous measurement of optoacoustic, absorbance, and fluorescence spectra. Herein, we employ MLS to analyze contrast agents (methylene blue, rhodamine 800, Alexa Fluor 750, IRDye 800CW, and indocyanine green) and proteins (sfGFP, mCherry, mKate, HcRed, iRFP720, and smURFP). We found that the absorption spectra do not correlate with the optoacoustic spectra for the majority of the analytes. We determined that for dyes, the transition underlying an aggregation state has more optoacoustic signal generation efficiency than the monomer transition. For proteins we found a favored optoacoustic relaxation that stems from the neutral or zwitterionic chromophores and unreported photoswitching behavior of tdTomato and HcRed. We then crystalized HcRed in its photoswitch optoacoustic state, confirming structurally the change in isomerization with respect to HcReds' fluorescence state. Finally, on the example of the widely used label tdTomato and the dye indocyanine green, we show the importance of correct photophysical (e.g., spectral and kinetic) information as a prerequisite for spectral-unmixing for in vivo imaging.

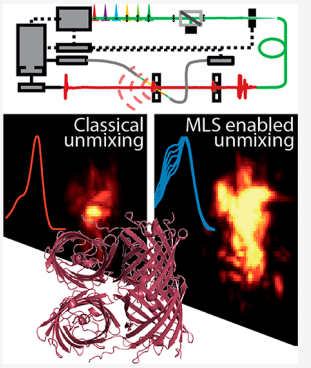

Optoacoustic (OA, also termed photoacoustic) imaging visualizes optical contrast with ultrasound resolution (Supporting Information 1), enabling high resolution, real-time *in vivo* imaging well-beyond the 1 mm penetration depth of typical optical methods.[1] Therefore, it is emerging as an appealing tool to study tumor biology,[2] inflammatory diseases,[3] or developmental processes.[4] However, in the majority of such studies, OA imaging relies entirely on endogenous absorbing-agents, like blood-hemoglobin, melanin, or lipids. In contrast, targeted labels enable longitudinal, cell-specific *in vivo* imaging, drastically expanding the potential applications of OA imaging.[5] Several potential agents have been tested for OA imaging, including nanoparticles and targeted dyes (reviewed in Gujrati et al., 2017[6]), as well as transgenic labels, such as fluorescent proteins and switchable bacteriophytochromes (reviewed in Brunker et al., 2017[7]).

Despite the fact that some labels were specifically developed for OA applications,[8,9] most label choices and strategies for their identification in images (unmixing) are based on photophysics inferred from independent transmission-mode absorption and fluorescence spectroscopy data, assuming convenient generalizability. As shown by our previous work, low quantum yield and high molar absorption do not automatically translate to a high optoacoustic signal.[10] In this work, we sought to develop a method of spectral analysis that combines absorption and fluorescence with OA spectral data to enable the full characterization of photophysical parameters of OA labels. Such a method helps to identify competing transitions; see Figure 1a. This data is a key to accelerate the tailored development of OA contrast agents and improve the identification of agents in imaging data. Lastly, a combined method of spectral analysis would enable the study of various photophysical phenomena simultaneously, such as the dye aggregation, exciton coupling, and energy conversion.

We introduce herein a multimodal laser spectrometer (MLS) that measures OA spectra with high precision and spectral resolution, concomitantly with absorption and fluorescence spectra. The high optoacoustic spectral quality, derived from a range of common dyes and chromoproteins, enables identifying significant differences between absorbance

Received: May 3, 2020
Accepted: July 8, 2020
Published: July 8, 2020

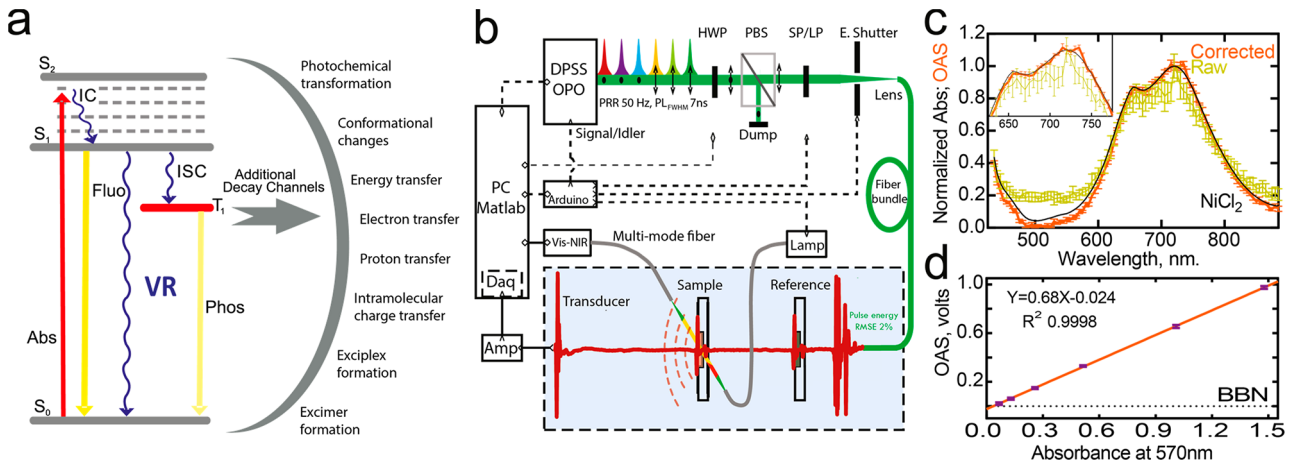

Figure 1. (a) Photophysics of OA signal generation together with common competing decay channels. Abs: absorbance, S_0: ground state, S_1: singlet excited state, T_1: triplet excited state, VR: vibrational relaxation, ISC: intersystem crossing, IC: internal conversion, Pho: phosphorescence, and Fluo: fluorescence. (b) MLS diagram. (c) Absorbance spectrum, raw, and corrected optoacoustic spectrum of $NiCl_2$. (d) Linear relation between absorbance and OA signal for brilliant black BN (BBN).

and OA spectra. We correlated these discrepancies either to an aggregation state of the dyes or to the isomeric state of the chromophores. Finally, we discuss how such high-quality MLS spectra can empower future optoacoustic contrast agent development and spectral unmixing to achieve high detection sensitivity in molecular imaging.

EXPERIMENTAL SECTION

Extended experimental details can be found in the Supporting Information.

Multimodality Laser Spectrometer (MLS). Based on expertise gained measuring the OA kinetic parameters of photocontrollable proteins,[11] we developed MLS (Figure 1b) that can record fluorescence, absorbance and high quality OA spectra simultaneously. An essential part of the MLS is a stepwise correction procedure enabling highly accurate OA spectral measurements (Figure 1c, and Supplementary Figures 1−5). Key characteristics of MLS are (i) illumination with pulsed lasers as in OA imaging; (ii) homogenized light fluence for all wavelengths; (iii) in-line reference to overcome laser instabilities; (iv) simultaneous detection of fluorescence excited by the laser pulse; and (v) simultaneous absorbance measurement. In contrast to other devices for recording OA spectra, which required samples with high concentrations and/or large volumes,[12−14] our MLS requires only 100 μL of minimum 0.2 optical density (OD) concentration for high-quality, reproducible spectra (Figure 1d).

Preparation of Dyes. Dyes were dissolved at 5 mg/ml in DMSO and frozen; prior to measurement, a stock solution of the dyes 1% v/v was prepared in 10% fetal bovine serum (FBS). The dye was further diluted to provide different concentrations. The absorbance spectra of each concentration were measured several times before experiments to ensure no change in the absorption spectra over time.

Preparation of Proteins. Proteins were expressed in *Escherichia coli* BL21 and purified by Ni-NTA affinity chromatography, followed by gel filtration on a HiLoad 26/600 Superdex 75pg column (Amersham Biosciences) in phosphate buffer saline (PBS) buffer. Purified proteins were frozen immediately in liquid nitrogen and stored at −80 °C. Thawed proteins were centrifuged at 14,000 rpm for 45 min at 4 °C, and the supernatant was used for the measurements.

Dextran Sodium Sulfate (DSS) Colitis Model and Sample Preparation. Colon inflammation was induced in reporter mice expressing tdTomato under control of the collagen VI promoter as previously described.[15] Mice were euthanized at day 8, when the entire colon was removed and incubated in Roti-Histofix overnight at 4 °C, before proceeding to the measurements.

Multi Spectral OA Tomography (MSOT). Colitis model MSOT images were obtained from excised colons on top of agar. The sample was illuminated by nanosecond pulses at 1 Hz from a tunable laser (Spitlight-DPSS 250 ZHG-OPO, InnoLas) Ultrasonic detection was performed using a curved 64-element array with a central frequency of 5 MHz (Imasonic SAS, Voray, France). Ultrasound data was reconstructed to images using a model-based approach.

ICG MSOT data has been recorded using the MSOT inVision 256 (iThera Medical GmbH). MSOT spectra between 680 and 900 nm of freshly euthanized mouse filled rectally with ICG solution 65 μM were recorded. IThera software ViewMSOT was used for image reconstruction and AMF-spectral unmixing using the ICG absorption and each of our ICG OA spectra.

Crystal Structure of HcRed. HcRed was purified as described above. The pure protein was exchanged from PBS to TRIS buffer pH 8.0 containing 300 mM NaCl and concentrated to 5 mg/mL. HcRed crystals grew in 0.1 M BICINE pH 8.5, 22% w/v polyethylene glycol 10,000. X-ray diffraction data set for HcRed was collected to 2.3 Å resolution.

RESULTS AND DISCUSSION

Characterization of Dyes. *Methylene Blue and Rhodamine 800.* The sensitivity to aggregation of some natural chromophores and organic dyes has been exploited for various sensing applications in OA imaging.[16,17] However, the photophysics underlying the OA signal changes have never been thoroughly understood, precluding efficient exploitation of such effects for the design of next-generation functional OA labels. Methylene Blue (MB) has been commonly employed as a label in OA.[18] Rhodamine 800 (Rh800) would be even more favorable for OA imaging due to its more pronounced red absorption (682 nm vs 660 nm of MB); however, it has a

https://dx.doi.org/10.1021/acs.analchem.0c01902
Anal. Chem. XXXX, XXX, XXX−XXX

strong fluorescence at 712 nm.[19] Both dyes, depending on environmental conditions like pH, ionic strength, and crowding agents, form self-aggregates through strong aromatic interactions.[20] In order to create a commonly defined medium for our measurements that resemble the cellular environment, we dissolved the dyes in PBS containing 10% FBS.[21] In this environment, all dyes are in a mixed aggregation state. Even more critically, this provides stable environments that enable us to observe the spectra without changes over time.

For solutions of MB with concentrations ranging from 17 to 29 μM, we found fluorescence emission only from excitation of the red-shifted spectral band, corresponding to the fluorescent monomer, while the blue-shifted band, associated predominantly with the H-aggregates (dye molecules stacked in the same orientation), did not show fluorescence (Figure 2a).

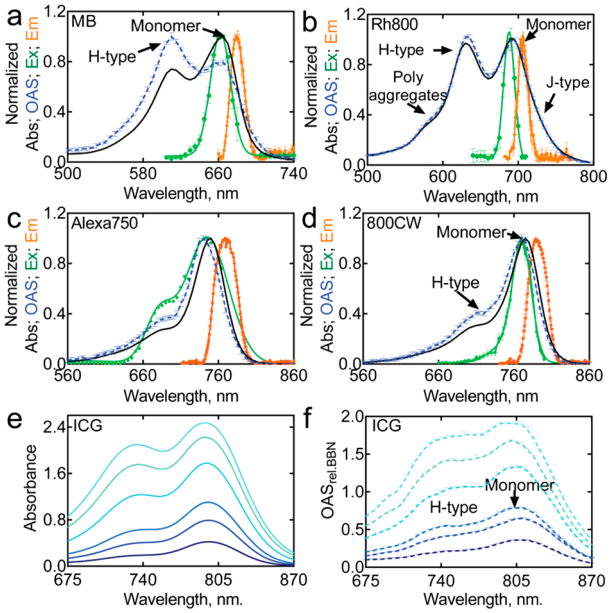

Figure 2. Normalized optoacoustic signal (OAS), absorption (Abs), emission (Em), and excitation (Ex) spectra for (a) MB, methylene blue; (b) Rh800, Rhodamine 800; (c) Alexa780, Alexa Fluor 750, and (d) 800CW, IRD$_{ye}$ 800CW. (e) Absorption and (f) optoacoustic spectra of ICG at increasing concentrations.

Conversely, the OA spectrum shows a stronger signal for the H-aggregate band (610 nm), reflecting a higher optoacoustic (photoacoustic signal generation efficiency, PGE, see Supplementary Text 1) for this transition compared to the monomer (slope of 0.61 at 610 nm vs 0.37 at 665 nm in Supplementary Figure 6a). It is generally accepted that the loss of fluorescence in highly symmetric H-aggregates, like the one formed by MB, stems from a favored ISC[22] (Supplementary Figure 7). This is corroborated by our photofatigue analysis, which shows faster bleaching for the H-aggregate at 610 nm (Supplementary Figure 8a) than for the monomer at 665 nm. It is commonly held that the vibronic relaxation following ISC, occurring in the long microseconds range, was considered too slow to contribute to detectable OA signals[23] in our observation time window of submicroseconds range and thus would not explain the higher PGE of the H-aggregate. Interestingly the ISC for MB is very fast (ns vs μs),[22] suggesting direct OA detection of the resultant vibronic relaxations. Consequently, we show here that the formation of H-aggregates by MB results in fast ISC, which contributes to the observed strengthening of the OA signal.

Dye Rh800 has thus far not been considered for applications in OA; however, the increase in the PGE of MB that we observed upon its aggregation prompted us also to study the photophysics of Rh800. We measured Rh800 in a concentration range from 30 to 49 μM. Rh800 shows a similar combination of monomer (695 nm) and predominantly H-aggregate (635 nm) bands, similar to MB (Figure 2b). But the Rh800 PGEs at the two bands are only slightly different (1.14 and 1.08, Supplementary Figure 6b). To our surprise, the PGE of the monomer form is higher than our standard BBN (Figure 1d), despite its fluorescence, while the bleaching rates of both transitions are moderate and suggest no strong ISC (Supplementary Table 1, Supplementary Figure 8b). The MLS spectra in Figure 2b showed that the fluorescence excitation spectrum is shifted relative to the absorbance peak at 695 nm, indicating a third transition, presumably a non-fluorescent J-aggregate (720 nm, arrow). Further inspection of the spectra reveals an additional shoulder around 580 nm (Figure 2b arrow). Such high energy transitions in xanthene dyes are often correlated with higher-order aggregates.[24] Given also a pronounced H-aggregate band suggests that most of the dye is in an aggregate state.

The acoustic wave for Rh800 at 695nm differs from the one at 635 nm and also from the one of BBN (Supplementary Figure 9). It is likely that this change of the acoustic wave is directly related to the higher-order aggregates. First, the aggregates represent a larger emitter changing the waveform, and second, the aggregates displace the water around the individual dye monomers and thus change the Grüneisen parameter. Both mechanisms favor the OA signals upon deexcitation, thus explaining the unusually high PGE.

Alexa Fluor 750 and IRDye 800CW. Alexa Fluor 750 (Alexa750) and IRDye 800CW (800CW) show absorbance peaks centered in the favorable blood window (749 and 774 nm, Figure 2c,d), which is why they have been developed for in vivo fluorescence imaging. Despite their relatively high fluorescence (quantum yields QY$_{fluo}$ = 0.12), both dyes have been used in OA imaging.[25,26]

Analysis of the spectra of Alexa750 shows a shift for the excitation maximum as well as the PGE maximum of 10 nm relative to the absorbance spectrum. This points to the OA transition at ~ 698 nm (Figure 2c), blue shoulder, arrow A). Additionally, this shoulder bleaches less than the main peak, with only 40% loss versus 80% after 60000 light pulses for the shoulder and main peak, respectively (Supplementary Figure 8c). This low bleaching and effective deexcitation in comparison to the main peak of Alexa750 points to a strong triplet tendency of the main peak leaving the transition at ~ 698 nm as the more effective one for imaging. Similar to the xanthene dyes, the absorbance spectrum of 800CW has two peaks (Figure 2d) with one centered at 710 nm and the second one centered at 770 nm. The excitation spectrum mirrors the primary absorption peak (770 nm), with a stronger PGE in the blue shoulder (710 nm), attributable to H-aggregates. Despite evidence of 800CW showing excitation coupling with other aromatic dyes,[27] there is no description in the literature of self-aggregation of 800CW. The observed behavior, spectrally similar to MB and Rh800 described above, might point to the blue shoulder resulting from H-type aggregation for 800CW. Intuitively, the formation of self-aggregates in 800CW seems to be unfavorable due to 800CW's strong negative character (four

https://dx.doi.org/10.1021/acs.analchem.0c01902
Anal. Chem. XXXX, XXX, XXX−XXX

negatively charged sulfonate groups). However, it has been noted that several other similarly charged dyes undergo aggregation and exciton coupling in the presence of macromolecules.[28] Thus, the FBS that is present in our solutions could lead to the formation of H-aggregates of 800CW, explaining the observed exciton coupling behavior.

Indocyanine Green. Indocyanine green (ICG) is a dye widely used in OA due to its strong signal intensity, favorable absorbance at 800 nm, and FDA approval.[29−32] However, the zwitterionic and hydrophobic character of ICG promotes aggregation at very low concentrations.[33,34] Thus photophysical properties of ICG vary with concentration, but also with the surrounding proteins that can modify its aggregation state.[21,34]

OA and absorbance spectra show a constant mismatch (Figure 2e,f), with the whole spectral shape exhibiting a redshift and an increase of the 745 nm band with increasing concentration. The PGE for the OA shoulder at 745 nm is 0.80. Interestingly the absorbance at 795 nm does not correlate linearly with the OAS (Supplementary Figure 10a). To compensate for this nonlinear behavior, we used two windows for the calculation of the PGEs, allowing a segmented linear fit (Supplementary Figure 10a). The PGE at 795 nm (0.62) is significantly lower at concentrations below 10 μM than it is above 10 μM (0.87), suggesting a higher PGE for aggregates of ICG. Thus, the difference between the dimer/monomer ratio from absorbance and OA represents the aggregation tendency of ICG (Supplementary Figure 10b). The PGE increases at the monomer peak (795 nm) with increasing concentration because the fraction of ICG aggregates also absorb at this wavelength. The discrepancies between absorbance and OA spectra observed could arise from different species of ICG present primarily at low concentrations, such as monomer, monomer bound to proteins (FBS), dimer, and dimer bound to proteins, as previously suggested.[34] At higher concentrations, aggregated ICG interacting with proteins becomes the predominant species, the OA and absorption spectra of which do not vary significantly. Our results for ICG prove clearly that aggregation increases optoacoustic signal generation. Beyond encouraging the production of nanoparticles with highly aggregated ICG for optoacoustic imaging, this also suggests the use of the aggregation states as ratiometric readout.

Characterization of Proteins. Genetically encoded labels are a prerequisite for longitudinal imaging and one of the reasons for fluorescence imaging becoming a standard tool in life sciences. GFP-like labels are prominent in fluorescence imaging and have also been studied and employed as OA labels.[5,12,35] However, biliverdin bearing chromoproteins like bacteriophytochromes (BphPs) or phycobiliproteins (Pbp) are advantageous due to their near-infrared (NIR) absorbance.[10,36] The hydroxybenzylidene imidazolidone chromophores of GFP-like proteins share complex photophysics involving different protonation states of the chromophore (neutral, zwitterionic, and anionic) and a plethora of additional effects like excited-state proton transfer (ESPT) and long-lived dark states (often involving isomerization along the methine bridge). For a review, see Van Thor et al., 2009.[37]

Classical Fluorescent Proteins. We measured MLS spectra (Figure 3 and Supplementary Figure 11) for sfGFP (an advanced variant of the original Aequorea victoria GFP[38]), red mKate2,[39] mCherry,[40] tdTomato,[40] and far-red nonfluorescent HcRed.[41] Comparing their OA and absorption spectra reveals that the blue shoulder of the peak is pronounced in OA.

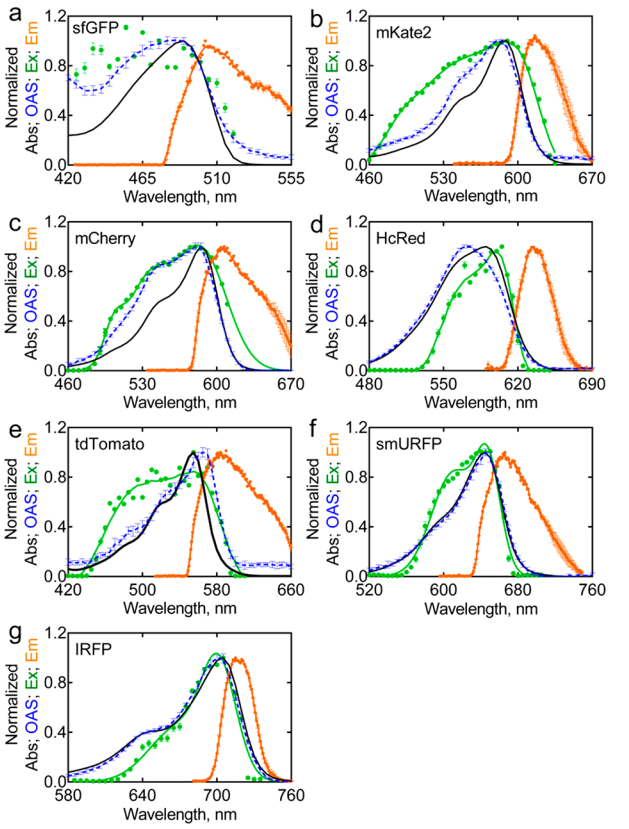

Figure 3. Normalized optoacoustic signal (OAS), absorption (Abs), emission (Em), and excitation (Ex) spectra for (a) sfGFP, (b) mKate2, (c) mCherry, (d) HcRed, (e) tdTomato, (f) smURFP, and (g) IRFP720 (IRFP). Linear relationship of OAS and Abs in Supplementary Figure 11.

Sometimes even leading to a blue-shift of the OA maxima compared to the absorption. sfGFP shows a maximum for absorbance and OA at 480 nm; however, the shoulder in the blue region of the OA spectra is more prominent, including an identifiable slope rising at ∼425 nm for the neutral chromophore (Figure 3a and in Supplementary Figure 11a). This is also reflected in a higher PGE for the blue transition compared to the main peak (425 nm: 0.75; 480 nm: 0.34). mKate2 has an optoacoustic spectrum that is 5 nm blue-shifted for the absorption spectra (585 nm vs 580 nm) and matching PGEs of 550 nm: 0.64 and 580 nm: 0.51 (Figure 3b and in Supplementary Figure 11b). For mCherry, the maximum is similarly blue-shifted compared to the absorbance (580 nm vs 585 nm) but with the corresponding PGE only slightly higher for the blue-shifted peak than for the absorbance peak (545 nm: 0.54; 585 nm: 0.53 (Figure 3c and in the Supplementary Figure 11c). For the far-red tetrameric protein HcRed, the optoacoustic spectrum is blue-shifted by 20 nm with respect to the absorption spectrum, with the peak center at 570 nm instead of 590 nm (Figure 3d and in Supplementary Figure 11d). Accordingly, the PGEs at 570 and 590 nm are 0.97 and 0.80, respectively.

In general, the PGEs of the main peaks are in good agreement with the reported fluorescent quantum yields (Supplementary Table 1). tdTomato however, a protein related to mCherry, showed an OA spectrum that is highly displaced to the red, a maximum in the OA spectrum at 565

https://dx.doi.org/10.1021/acs.analchem.0c01902
Anal. Chem. XXXX, XXX, XXX−XXX

nm, rather than 555 nm, with a PGE of 0.79 at 485 nm and of 0.83 at 565 nm (Figure 3e and Supplementary Figure 11e).

Several explanations are possible for the higher PGE of the blue shoulder observed in most of the proteins. (i) The blue shift could result from an involvement of the neutral state of the chromophore.[42,43] It is possible that the deexcitation from this state results in vibronic relaxation and a higher PGE. (ii) For HcRed, our data is in agreement with the theory of a mixture of cis−trans isomers, with a nonfluorescent, neutral trans-isomer centered at around 570 nm and a slightly fluorescent cis-isomer centered at 590 nm.[44] The high PGE from the peak at 570 nm could arise from the nonfluorescent properties of the trans-isomer. (iii) Discrepancies between OA and absorption spectra have been observed before and explained by ground state depopulation.[12] This effect primarily comes into play for the strongly absorbing main transitions leading to the "flattened" OA peaks observed by Laufer and colleagues.[12] Since in our study the discrepancies are regularly found at the flanks of the spectra or only for certain peaks (e.g., aggregate peaks or protonated chromophores), we believe that the phenomenon of ground state depopulation does not explain our results.

Near Infrared Fluorescent Proteins. Biliverdin binding proteins are of critical importance, as their absorption in the near-infrared region gives them superior penetration depth and spectral separation for endogenous contrast. Until now, only two classes of biliverdin binding proteins have been reported: bacteriophytochromes and phycobiliproteins.[45,46] IRFP720 and smURFP are examples of both classes. In both cases, the optoacoustic spectra match the absorption spectra, with PGEs of 0.56 and 0.86 for smURFP and IRFP720 at their primary OA peaks, respectively (Figure 3f,g). The lower PGE of smURFP correlates with its higher quantum yield 0.2 versus 0.06 for IRFP720. Additional reductions in PGE could come from faster bleaching and transient isomerization.[47]

Photoconversion in Classical Fluorescent Proteins. Unexpectedly MLS spectra of several proteins showed a level of photoconversion or photoswitching that was previously unknown. This was initially observed when comparing forward (420 to 900 nm) and reverse (900 to 420 nm) modes of collecting spectral data.

For mCherry and tdTomato, the effects are different but always show a long-lived change of the OA spectra. For mCherry, measuring from 420 to 900 nm results in a stronger blue shoulder than measuring in the opposite direction (Figure 4a). The absorption spectrum of mCherry does not change accordingly (Figure 4c), resulting in an increase of the PGE of the shoulder from 0.35 to 0.45).

While for tdTomato, measuring from reversed 900 to 420 nm results in a stronger blue shoulder, with a change in PGE for both peaks (Figure 4d and Suppl. Figure 11e), and red-shifted maxima of the OA spectra. Alternating illumination probing with 480 nm and photoconverting with 550 nm shows how the absorption spectra changed with an increase of the band at 480 nm, which can be attributed to the neutral chromophore in those proteins (Figure 4e,f). It could be that the effects in tdTomato under strong pulsed laser illumination are similar to photoswitching events in related rsCherry and rsCherryRev proteins,[48] although we see no dark-relaxation.

For the far-red protein HcRed, continuous illumination at 565 nm did not produce a decrease in OA intensity (bleaching) as expected but an increase in OA signal (Figure 4g−i). Alternating illumination between 565 and 590 nm

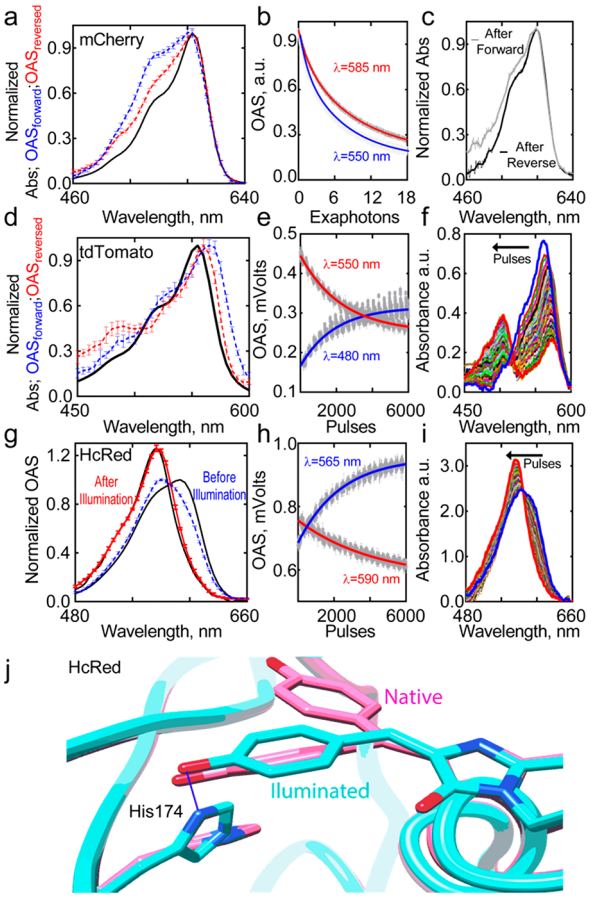

Figure 4. Photoswitching effects in mCherry, tdTomato, and HcRed. (a, d, and g) OA spectra from 900 to 420 nm (reverse, red) or 420 to 900 nm (forward, blue) along with the absorption spectra in the nonilluminated state. (b, e, and h) The temporal development of the OA signals at the two peaks. (c) mCherry absorption spectra before and after OA measurements; (f) tdTomato after pulses of 550/480 nm light, and (i) 590/565 nm light for HcRed, respectively. (j) In blue structure of HcRed after 60000 pulses of 565 nm light (6Y1G) and in pink structure of native HcRed (1YZW).

results in a reduction in the signal at the fluorescence peak at 590, but an increase at the optoacoustic peak at 565nm; the absorption spectra show the same kinetics. A published crystal structure of HcRed suggests inherent chromophore flexibility with the trans nonplanar isomer responsible for the shoulder at 570 nm, and cis-isomer responsible for the peak at 590 nm, with both conformer in equilibrium.[44]

In order to validate our proposed mechanism, we decided to crystalize our photoconverted version of HcRed. Our structure (PDB ID: 6Y1G, Supplementary Table 2) shows that the inherent chromophore flexibility is not present anymore after pulsed illumination (Figure 4j and Supplementary Figure 12). The new structure only has a trans-nonplanar chromophore that is tilted and stabilizes by a new H-bond with a twisted His174. Our structure corroborates that the trans-isomer is responsible for the optoacoustic peak in HcRed and support further our hypothesis that it is the trans chromophore responsible for the higher PGE of the shoulder for sfGFP, mKate2, and mCherry.

Spectral Insights to Improve Spectral Unmixing. Beyond clarifying fundamental photophysical mechanisms, our accurate OA spectroscopic investigations are immediately

https://dx.doi.org/10.1021/acs.analchem.0c01902
Anal. Chem. XXXX, XXX, XXX−XXX

beneficial to the improvement of in vivo imaging. To demonstrate this, we chose the dye ICG and the transgene reporter protein tdTomato since both are widely used labels in fluorescence and optoacoustic imaging. Numerous dye-labeling-procedures and transgenic animals are existing for ICG and tdTomato, respectively, which can immediately benefit from detection strategies improved by our spectral information.

As described above, ICG has various aggregation states with different optoacoustic spectra which depend not only on ICG concentration but also on its interacting partners (lipids, protein, etc.), leading to heterogeneity of ICG forms in the hard to define in vivo environment. Nonetheless, most (commercial) unmixing algorithms utilize only the absorption spectrum of diluted monomeric ICG for spectral unmixing (Figure 5a, 1). To illustrate the benefit of spectral-unmixing

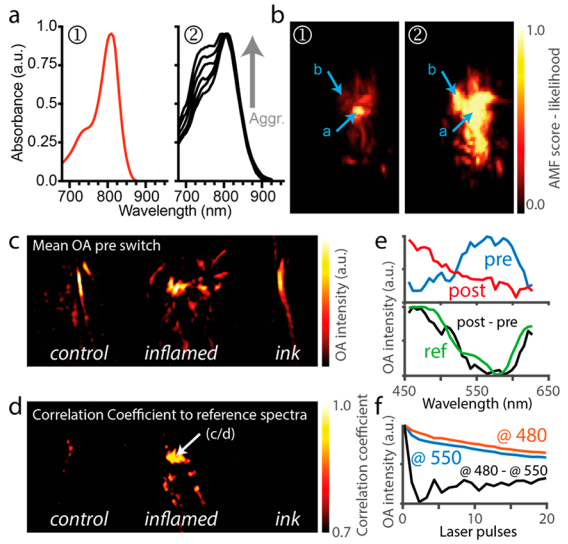

Figure 5. (a) ICG spectra used for AMF spectral unmixing in b. (1) Commonly used monomeric ICG absorption spectrum, (2) library of ICG optoacoustic spectra at different aggregation states obtained with the MLS. (b) MSOT images of a mouse colon with ICG solution. Unmixed with the spectra shown in a. Shown is a maximum intensity projection of all slices. (c) Visible OA tomography images of control colon and a colon with acute DSS-induced inflammation from tdTomatoColVI reporter mice. Shown is the mean signal at wavelengths from 450 to 650 nm. (d) tdTomato signal detection after photoconversion with multiple pulses of probing and photo converting illumination, followed by differential spectra unmixing. (e) Exemplary spectra before and after conversion (top) and difference spectra together with known difference spectra from MLS used as "search spectra" for the unmixing. (f) Photoconversion of tdTomato positive pixels showing the shift of the peak ratio upon.

with a number of OA spectra of different ICG aggregation states (Figure 5a, 2) we introduce a solution of ICG 65 μM rectally in a euthanized wildtype mouse scanned with multispectral optoacoustic tomography (MSOT). While unmixing using adaptive matched filter (AMF, ViewMOST 3.8.10.04, iThera Medical). Using the classical single absorption spectrum of ICG, we found only signals with a high confidence value in the center of the colon (Figure 5b, 1); the same procedure using ICG spectra of different aggregation states shows high-confidence unmixing in the complete colon (Figure 5b, 2). This is in line with the observation that different regions of the colon are differently picked up by individual spectra, suggesting differences in aggregation in those regions (Supplementary Figure 13). It is likely that ICG remains more diluted in the high-volume colon's lumen (arrow a), and it concentrates in the small volume colonics crypts (arrow b). Thus, unmixing with different ICG aggregation state spectra can additionally carry information on local aggregation states and might allow additional conclusions on the immediate environment in those regions as well as ICG concentration.

Spectral unmixing of tdTomato in OA imaging in vivo is not straightforward due to overlapping absorption with hemoglobin in tissue. We showed that the illumination used in MLS, which is similar to one used for OA imaging, is sufficient to induce a photoconversion of tdTomato. Using this insight and the knowledge on the spectra before and after photoconversion we could readily facilitate unmixing of tdTomato signals from colons. In short, we recorded uninflamed (control) or DSS-induced, inflamed colons from reporter mice expressing tdTomato under control of the collagen VI promoter (tdTomatoColVI).[15,49] We collected spectral data from 420 to 690 nm using a tomography style imaging device with a 64-element ultrasound transducer and 45° tilted illumination. We collected spectra before and after converting tdTomato with 80 cycles of 500 pulses of photo converting light (550nm) and 500 pulses of probing light (480nm). While the signal from blood made distinction between the inflamed and control colon difficult in plain OA imaging (Figure 5c); unmixing, based on the difference spectra (Figure 5e) allowed one to selectively visualize the inflamed colon (Figure 5d) reflecting accumulation and activation of colon fibroblasts and other COLVI (tdTomato) expressing cells in DSS-induced inflammatory lesions. Our results are in line with corresponding findings published before.[35,50] We note that also the conversion itself can be utilized if monitored by collecting data at the peak wavelengths 480 and 550 nm (Figure 5f).

CONCLUSION

Our first results using the MLS showed a wealth of insights into the behavior of a number of well-used dyes and proteins. Describing the exact changes in the photophysics of OA signal generation (Figure 1a and Supplementary Text 1) upon the aggregation of MB, Rh800, and ICG will afford new applications for sensors that exploit their environment-dependent aggregation, for example, ratiometric analysis of dye aggregation under different physiological conditions. Finally, our results on ICG shed light on the complex behavior of this molecule, which is so regularly used in OA studies.[29,30] Cognizance of the strong dependence of PGE on the aggregation of dyes could help researchers to analyze concentration-dependent measurements of ICG more accurately. On the protein side, the switching or conversion behavior of mCherry, tdTomato, and HcRed is extremely interesting for GFP-like protein research and warrants further study; however, it also has an immediate impact on employing those proteins in OA applications. In particular, tdTomato, for which there are numerous animal models from fluorescence studies, can be used more effectively for OA measurements by exploiting the transition from 550 to 480 nm and using a dual-wavelength ratio analysis to identify the protein-label in tissue with a strongly absorbing background.

Lastly, we could show that accurate measurements for OA labels are a prerequisite for their understanding, their future design, and especially their comparison. With regard to this, the use of standards like BBN for novel OA contrast agents to

https://dx.doi.org/10.1021/acs.analchem.0c01902
Anal. Chem. XXXX, XXX, XXX−XXX

come is highly important for comparability and for empowering researchers to make strategic choices on what labels to use in their experiments.

■ ASSOCIATED CONTENT

Supporting Information

The Supporting Information is available free of charge at https://pubs.acs.org/doi/10.1021/acs.analchem.0c01902.

Extended introduction and methods, process diagrams for the analysis, further OA data and structural data for HcRed (PDF)

■ AUTHOR INFORMATION

Corresponding Author

Andre C. Stiel − *Institute of Biological and Medical Imaging (IBMI), Helmholtz Zentrum München, D-85764 Neuherberg, Germany;* orcid.org/0000-0001-8675-6797; Email: andre.stiel@helmholtz-muenchen.de

Authors

Juan Pablo Fuenzalida Werner − *Institute of Biological and Medical Imaging (IBMI), Helmholtz Zentrum München, D-85764 Neuherberg, Germany;* orcid.org/0000-0001-6651-3851

Yuanhui Huang − *Institute of Biological and Medical Imaging (IBMI), Helmholtz Zentrum München, D-85764 Neuherberg, Germany; Chair of Biological Imaging, Technische Universitat München, D-81675 Munich, Germany;* orcid.org/0000-0002-4774-7449

Kanuj Mishra − *Institute of Biological and Medical Imaging (IBMI), Helmholtz Zentrum München, D-85764 Neuherberg, Germany; Chair of Biological Imaging, Technische Universitat München, D-81675 Munich, Germany*

Robert Janowski − *Intracellular Transport and RNA Biology Group, Institute of Structural Biology, Helmholtz Zentrum München, D-85764 Neuherberg, Germany*

Paul Vetschera − *Institute of Biological and Medical Imaging (IBMI), Helmholtz Zentrum München, D-85764 Neuherberg, Germany; Chair of Biological Imaging, Technische Universitat München, D-81675 Munich, Germany*

Christina Heichler − *First Department of Medicine, Universitaetsklinikum Erlangen, Friedrich-Alexander-Universitaet Erlangen-Nuernberg, 91054 Erlangen, Germany*

Andriy Chmyrov − *Institute of Biological and Medical Imaging (IBMI), Helmholtz Zentrum München, D-85764 Neuherberg, Germany; Chair of Biological Imaging and Center for Translational Cancer Research (TranslaTUM), Technische Universitat München, D-81675 Munich, Germany;* orcid.org/0000-0003-0265-019X

Clemens Neufert − *First Department of Medicine, Universitaetsklinikum Erlangen, Friedrich-Alexander-Universitaet Erlangen-Nuernberg, 91054 Erlangen, Germany*

Dierk Niessing − *Intracellular Transport and RNA Biology Group, Institute of Structural Biology, Helmholtz Zentrum München, D-85764 Neuherberg, Germany; Institute of Pharmaceutical Biotechnology, Ulm University, 89081 Ulm, Germany*

Vasilis Ntziachristos − *Institute of Biological and Medical Imaging (IBMI), Helmholtz Zentrum München, D-85764 Neuherberg, Germany; Chair of Biological Imaging and Center for Translational Cancer Research (TranslaTUM), Technische Universitat München, D-81675 Munich, Germany*

Complete contact information is available at: https://pubs.acs.org/10.1021/acs.analchem.0c01902

Author Contributions

J.P.F.W. and Y.H. contributed equally. J.P.F.W. and Y.H. built the MLS with help from P.V. in early stages. Y.H. programmed the measurement routine. J.P.F.W., Y.H., and K.M. conducted measurements. R.J. solved the structure. A.C., C.N., D.N., and V.N. contributed to the manuscript. C.K. conducted the colon preparation. A.C.S. J.P.F.W., and Y.H. wrote the manuscript and devised the project. All authors approved the manuscript.

Notes

The authors declare the following competing financial interest(s): VN is a shareholder of iThera Medical.

■ ACKNOWLEDGMENTS

The authors want to thank Hong Yang, Dr. Ara Ghazaryan, Dr. Yu-Shan Huang, Dr. Christian Zakian, Dr. Jan G. Laufer for discussions, Sarah Glasl for help with experiments, Jessica Klausmann for technical help, and G. Kollias for providing ColVI-Cre mice.

■ REFERENCES

(1) Ntziachristos, V. *Nat. Methods* **2010**, *7* (8), 603−614.

(2) Omar, M.; Schwarz, M.; Soliman, D.; Symvoulidis, P.; Ntziachristos, V. *Neoplasia* **2015**, *17* (2), 208−214.

(3) Aguirre, J.; Schwarz, M.; Garzorz, N.; Omar, M.; Buehler, A.; Eyerich, K.; Ntziachristos, V. *Nat. Biomed. Eng.* **2017**, *1*, 68.

(4) Vetschera, P.; Koberstein-Schwarz, B.; Schmitt-Manderbach, T.; Dietrich, C.; Hellmich, W.; Chekkoury, A.; Symvoulidis, P.; Reber, J.; Westmeyer, G.; López-Schier, H.; Omar, M.; Ntziachristos, V. Beyond Early Development: Observing Zebrafish over 6 Weeks with Hybrid Optical and Optoacoustic Imaging. *BioRxiv*; **2019**, DOI: 10.1101/586933.

(5) Razansky, D.; Distel, M.; Vinegoni, C.; Ma, R.; Perrimon, N.; Köster, R. W.; Ntziachristos, V. *Nat. Photonics* **2009**, *3* (7), 412−417.

(6) Gujrati, V.; Mishra, A.; Ntziachristos, V. *Chem. Commun.* **2017**, *53* (34), 4653−4672.

(7) Brunker, J.; Yao, J.; Laufer, J.; Bohndiek, S. E. *J. Biomed. Opt.* **2017**, *22* (7), 070901.

(8) Mishra, K.; Stankevych, M.; Fuenzalida-Werner, J. P.; Grassmann, S.; Gujrati, V.; Huang, Y.; Klemm, U.; Buchholz, V. R.; Ntziachristos, V.; Stiel, A. C. *Sci. Adv.* **2020**, *6*, eaaz6293.

(9) Chee, R. K. W.; Li, Y.; Zhang, W.; Campbell, R. E. *J. Biomed. Opt.* **2018**, *23* (10), 1.

(10) Fuenzalida Werner, J. P. J. P.; Mishra, K.; Huang, Y.; Vetschera, P.; Glasl, S.; Chmyrov, A.; Richter, K.; Ntziachristos, V.; Stiel, A. C. *ACS Chem. Biol.* **2019**, *14* (9), 1896−1903.

(11) Vetschera, P.; Mishra, K.; Fuenzalida-Werner, J. P.; Chmyrov, A.; Ntziachristos, V.; Stiel, A. C. *Anal. Chem.* **2018**, *90* (17), 10527−10535.

(12) Laufer, J.; Jathoul, A.; Pule, M.; Beard, P. *Biomed. Opt. Express* **2013**, *4* (11), 2477.

(13) Teng, Y. C.; Royce, B. S. H. *J. Opt. Soc. Am.* **1980**, *70*, 557.

(14) Schneider, S.; Coufal, H. *J. Chem. Phys.* **1982**, *76*, 2919.

(15) Wirtz, S.; Neufert, C.; Weigmann, B.; Neurath, M. F. *Nat. Protoc.* **2007**, *2* (3), 541−546.

(16) Peters, L.; Weidenfeld, I.; Klemm, U.; Loeschcke, A.; Weihmann, R.; Jaeger, K. E.; Drepper, T.; Ntziachristos, V.; Stiel, A. C. *Nat. Commun.* **2019**, *10* (1), 1−9.

(17) Wang, J.; Jeevarathinam, A. S.; Humphries, K.; Jhunjhunwala, A.; Chen, F.; Hariri, A.; Miller, B. R.; Jokerst, J. V. *Bioconjugate Chem.* **2018**, *29* (11), 3768−3775.

(18) Taruttis, A.; Ntziachristos, V. *Nat. Photonics* **2015**, *9* (4), 219−227.

(19) Alessi, A.; Salvalaggio, M.; Ruzzon, G. *J. Lumin.* **2013**, *134*, 385−389.
(20) Moreno-Villoslada, I.; Fuenzalida, J. P.; Tripailaf, G.; Araya-Hermosilla, R.; Pizarro, G. D. C.; Marambio, O. G.; Nishide, H. *J. Phys. Chem. B* **2010**, *114* (37), 11983−11992.
(21) Bongsu Jung; Vullev, V. I.; Anvari, B. *IEEE J. Sel. Top. Quantum Electron.* **2014**, *20* (2), 149−157.
(22) Morgounova, E.; Shao, Q.; Hackel, B. J.; Thomas, D. D.; Ashkenazi, S. *J. Biomed. Opt.* **2013**, *18* (5), 056004.
(23) Schaberle, F. A.; Rego Filho, F. D. A. M. G. G.; Reis, L. A.; Arnaut, L. G. *Photochem. Photobiol. Sci.* **2016**, *15* (2), 204−210.
(24) Moreno-Villoslada, I.; Torres-Gallegos, C.; Araya-Hermosilla, R.; Nishide, H. *J. Phys. Chem. B* **2010**, *114* (12), 4151−4158.
(25) Lakshman, M.; Needles, A. *Nat. Methods* **2015**, *12* (4), No. iii.
(26) Chen, Z.; Deán-Ben, X. L.; Gottschalk, S.; Razansky, D. *Biomed. Opt. Express* **2018**, *9* (5), 2229−2239.
(27) Zhang, J.; Smaga, L. P.; Satyavolu, N. S. R.; Chan, J.; Lu, Y. *J. Am. Chem. Soc.* **2017**, *139* (48), 17225−17228.
(28) Hoffmann, S.; Fuenzalida Werner, J. P.; Moreno-Villoslada, I.; Goycoolea, F. M. New Insights into the Nature of the Cibacron Brilliant Red 3B-A - Chitosan Interaction. In *Pure and Applied Chemistry*; Walter de Gruyter GmbH, 2016; Vol. *88*, pp 891−904.
(29) Beziere, N.; Lozano, N.; Nunes, A.; Salichs, J.; Queiros, D.; Kostarelos, K.; Ntziachristos, V. *Biomaterials* **2015**, *37*, 415−424.
(30) Wilson, K. E.; Bachawal, S. V; Willmann, J. K. *Clin. Cancer Res.* **2018**, *24* (15), 3572−3582.
(31) Weber, J.; Beard, P. C.; Bohndiek, S. E. *Nat. Methods* **2016**, *13* (8), 639−650.
(32) Kim, C.; Song, K. H.; Gao, F.; Wang, L. V. *Radiology* **2010**, *255* (2), 442−450.
(33) Zweck, J.; Penzkofer, A. *Chem. Phys.* **2001**, *269* (1−3), 399−409.
(34) Philip, R.; Penzkofer, A.; Bäumler, W.; Szeimies, R. M.; Abels, C. *J. Photochem. Photobiol., A* **1996**, *96* (1−3), 137−148.
(35) Scheibe, K.; Kersten, C.; Schmied, A.; Vieth, M.; Primbs, T.; Carlé, B.; Knieling, F.; Claussen, J.; Klimowicz, A. C.; Zheng, J.; Baum, P.; Meyer, S.; Schürmann, S.; Friedrich, O.; Waldner, M. J.; Rath, T.; Wirtz, S.; Kollias, G.; Ekici, A. B.; Atreya, R.; Raymond, E. L.; Mbow, M. L.; Neurath, M. F.; Neufert, C. *Gastroenterology* **2019**, *156* (4), 1082−1097.
(36) Li, L.; Shemetov, A. A.; Baloban, M.; Hu, P.; Zhu, L.; Shcherbakova, D. M.; Zhang, R.; Shi, J.; Yao, J.; Wang, L. V; Verkhusha, V. V. *Nat. Commun.* **2018**, *9* (1), 2734.
(37) Van Thor, J. J. *Chem. Soc. Rev.* **2009**, *38* (10), 2935−2950.
(38) Pédelacq, J.-D.; Cabantous, S.; Tran, T.; Terwilliger, T. C.; Waldo, G. S. *Nat. Biotechnol.* **2006**, *24* (1), 79−88.
(39) Shcherbo, D.; Murphy, C. S.; Ermakova, G. V; Solovieva, E. A.; Chepurnykh, T. V; Shcheglov, A. S.; Verkhusha, V. V; Pletnev, V. Z.; Hazelwood, K. L.; Roche, P. M.; Lukyanov, S.; Zaraisky, A. G.; Davidson, M. W.; Chudakov, D. M. *Biochem. J.* **2009**, *418* (3), 567−574.
(40) Shaner, N. C.; Campbell, R. E.; Steinbach, P. a; Giepmans, B. N. G.; Palmer, A. E.; Tsien, R. Y. *Nat. Biotechnol.* **2004**, *22* (12), 1567−1572.
(41) Gurskaya, N. G. N. G.; Fradkov, A. F. A. F.; Terskikh, A.; Matz, M. V; Labas, Y. A.; Martynov, V. I.; Yanushevich, Y. G.; Lukyanov, K. A.; Lukyanov, S. A. *FEBS Lett.* **2001**, *507*, 16−20.
(42) Cotlet, M.; Hofkens, J.; Maus, M.; Gensch, T.; Van der Auweraer, M.; Michiels, J.; Dirix, G.; Van Guyse, M.; Vanderleyden, J.; Visser, A. J. W. G.; De Schryver, F. C. *J. Phys. Chem. B* **2001**, *105* (21), 4999−5006.
(43) Miyawaki, A. *Nat. Biotechnol.* **2004**, *22* (11), 1374−1376.
(44) Wilmann, P. G.; Petersen, J.; Pettikiriarachchi, A.; Buckle, A. M.; Smith, S. C.; Olsen, S.; Perugini, M. a.; Devenish, R. J.; Prescott, M.; Rossjohn, J. *J. Mol. Biol.* **2005**, *349*, 223−237.
(45) Shcherbakova, D. M.; Verkhusha, V. V. *Nat. Methods* **2013**, *10* (8), 751−754.
(46) Rodriguez, E. A.; Tran, G. N.; Gross, L. A.; Crisp, J. L.; Shu, X.; Lin, J. Y.; Tsien, R. Y. *Nat. Methods* **2016**, *13* (9), 763−769.
(47) Braslavsky, S. E.; Ellul, R. M.; Weiss, R. G.; Al-Ekabi, H.; Schaffner, K.; Alekabi, H.; Schaffner, K.; Al-Ekabi, H.; Schaffner, K.; Silvia, E.; Braslavsky Richard, G. Weiss; Hussain Al-Ekabi; Kurt Schaffner, R. M. E. *Tetrahedron* **1983**, *39* (11), 1909−1913.
(48) Stiel, A. C.; Andresen, M.; Bock, H.; Hilbert, M.; Schilde, J.; Schönle, A.; Eggeling, C.; Egner, A.; Hell, S. W. S. W.; Jakobs, S. *Biophys. J.* **2008**, *95* (6), 2989−2997.
(49) Heichler, C.; Scheibe, K.; Schmied, A.; Geppert, C. I.; Schmid, B.; Wirtz, S.; Thoma, O.-M.; Kramer, V.; Waldner, M. J.; Büttner, C.; Farin, H. F.; Pešić, M.; Knieling, F.; Merkel, S.; Grüneboom, A.; Gunzer, M.; Grützmann, R.; Rose-John, S.; Koralov, S. B.; Kollias, G.; Vieth, M.; Hartmann, A.; Greten, F. R.; Neurath, M. F.; Neufert, C. *Gut* **2020**, *69*, 1269.
(50) Knieling, F.; Gonzales Menezes, J.; Claussen, J.; Schwarz, M.; Neufert, C.; Fahlbusch, F. B.; Rath, T.; Thoma, O. M.; Kramer, V.; Menchicchi, B.; Kersten, C.; Scheibe, K.; Schürmann, S.; Carlé, B.; Rascher, W.; Neurath, M. F.; Ntziachristos, V.; Waldner, M. J. *Gastroenterology* **2018**, *154*, 807.

https://dx.doi.org/10.1021/acs.analchem.0c01902
Anal. Chem. XXXX, XXX, XXX−XXX